Vujovic *et al. Cell Communication and Signaling* (2024) 22:450
https://doi.org/10.1186/s12964-024-01825-1

Cell Communication and Signaling

RESEARCH Open Access

Mitochondria facilitate neuronal differentiation by metabolising nuclear-encoded RNA

Filip Vujovic[1,2], Mary Simonian[1], William E. Hughes[3], Claire E. Shepherd[4], Neil Hunter[1] and Ramin M. Farahani[1,2*]

Abstract

Mitochondrial activity directs neuronal differentiation dynamics during brain development. In this context, the long-established metabolic coupling of mitochondria and the eukaryotic host falls short of a satisfactory mechanistic explanation, hinting at an undisclosed facet of mitochondrial function. Here, we reveal an RNA-based inter-organellar communication mode that complements metabolic coupling of host-mitochondria and underpins neuronal differentiation. We show that within minutes of exposure to differentiation cues and activation of the electron transport chain, the mitochondrial outer membrane transiently fuses with the nuclear membrane of neural progenitors, leading to efflux of nuclear-encoded RNAs (neRNA) into the positively charged mitochondrial intermembrane space. Subsequent degradation of mitochondrial neRNAs by Polynucleotide phosphorylase 1 (PNPase) located in the intermembrane space curbs the transcriptomic memory of progenitor cells. Further, acquisition of neRNA by mitochondria leads to a collapse of proton motive force, suppression of ATP production, and a resultant amplification of autophagic flux that attenuates proteomic memory. Collectively, these events force the progenitor cells towards a "tipping point" characterised by emergence of a competing neuronal differentiation program. It appears that neuronal differentiation is a consequence of reprogrammed coupling of metabolomic and transcriptomic landscapes of progenitor cells, with mitochondria emerging as key "reprogrammers" that operate by acquiring and metabolising neRNAs. However, the documented role of mitochondria as "reprogrammers" of differentiation remains to be validated in other neuronal lineages and in vivo.

Introduction

Accumulating evidence suggests that mitochondrial dynamics and neuronal differentiation are intimately linked [1–5]. There appears to be a critical temporal window, shortly after exposure of neural progenitor cells to differentiation cues, wherein the fate of mitochondria accurately anticipates the fate of the eukaryotic cell [1]. In this restricted temporal window, a diminished mitochondrial population and a shift to glycolytic metabolism characterise progenitor cells that continue self-renewal, and vice versa [1]. Likewise, amplification of mitochondrial activity by cannibalisation of heme-rich erythroblasts accelerates neuronal differentiation during

*Correspondence:
Ramin M. Farahani
ramin.mostofizadehfarahani@sydney.edu.au
[1]IDR/WSLHD Research and Education Network, Sydney, NSW 2145, Australia
[2]School of Medical Sciences, Faculty of Medicine and Health, University of Sydney, Sydney, NSW 2006, Australia
[3]Children's Medical Research Institute, Sydney, NSW 2145, Australia
[4]Neuroscience Research Australia, Sydney, NSW 2031, Australia

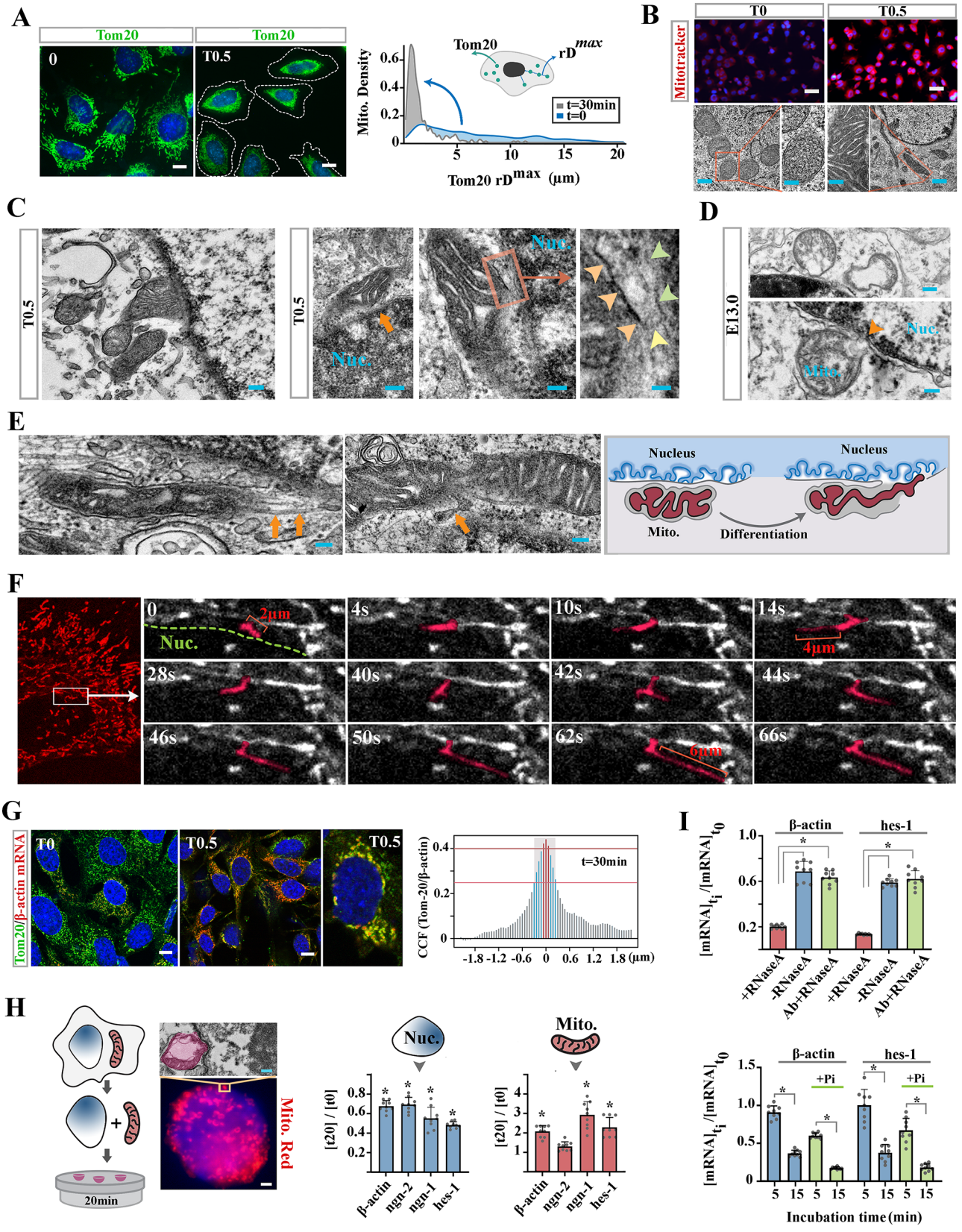

Fig. 1 (See legend on next page.)

(See figure on previous page.)

Fig. 1 Mitochondria of NPCs acquire neRNAs upon induction of neuronal differentiation. (**A**) Immunohistochemical staining of mitochondrial outer membrane transporter Tom20 at t = 0 and t = 0.5 h post-induction of differentiation (Scale bars: 8 µm, see Supplementary Fig. S1 for detail). Right graph shows maximum radial distance (rD^{max}) between $Tom20^+$ mitochondria and the nuclear membrane measured at uniform intervals covering the entire perimeter of individual cells ($n = 36$ rD^{max}/cell). (**B**) Top photomicrographs show mitochondrial membrane potential probed by MitoTracker Red (conc. 50nM) in control NPCs (T0) and 0.5 h post-induction of differentiation (T0.5 h). Bottom representative electron microscopy photomicrographs demonstrate the enhanced electron density and the structural maturation of the mitochondrial cristae in differentiating NPCs (0.5 h, T05, right) as opposed to control cells (T0, left). Scale bars top: 40 µm, bottom left: 0.5 µm, bottom insets: 0.2 µm, bottom right: 1 µm. (**C**) Representative electron microscopy photomicrographs show key ultrastructural features of neural progenitor cells 0.5 h (T0.5) after exposure to differentiation cues in vitro. Note the continuity of mitochondrial outer membrane and nuclear membrane (arrowheads) in NPCs 0.5 h (T0.5) post-induction of differentiation. Scale bars left: 0.2 µm, middle: 0.25 µm, right: 80 nm, inset: 20 nm. (**D**) Electron microscopy photomicrographs show the relationship between mitochondria and nuclei in differentiating neural progenitor cells in a rostral region of developing (E13) mouse neural tube. Scale bars top: 0.3 µm, bottom: 0.1 µm. **(E)** Representative electron microscopy photomicrographs show extrusions of mitoplast (orange arrows) extended through the fusion pore towards the chromatin. Scale bars left: 0.2 µm, right: 0.15 µm. The schematic image illustrates extrusion of a mitoplast towards the nucleus upon induction of differentiation. (**F**) Left photomicrograph shows distribution of $PKMO^+$ mitochondria upon induction of differentiation, captured via live-cell TauSTED nanoscopy. The inset shows dynamics of a pseudo-coloured $PKMO^+$ mitochondrion post-induction of differentiation (see supplementary Movie S1). (**G**) Photomicrograph shows double IHC/FISH staining of mitochondria for Tom20 (green) and β-actin neRNA (red) at baseline (T0) and 0.5 h after induction of differentiation. Graph shows linear Spearman cross-correlation between intensities of green (Tom20) and red (β-actin neRNA) fluorescence signals measured radially at 36 intervals covering the entire perimeter of individual cells. (**H**) In the 3D organellar co-incubation method, isolated mitochondria and nuclei were mixed and co-incubated in a suspended mode in a drop of RNase-free IB_c buffer in order to maximise the interaction of mitochondria and nuclei. Top micrograph shows the assembly of isolated mitochondria labelled with Mitotracker Red (50nM) and an isolated $DAPI^+$ nucleus generated via the organellar co-incubation method. A corresponding electron photomicrograph shows an isolated mitochondrion communicating with an isolated nucleus. After 20 min mitochondria and nuclei were separated using a sucrose gradient (see methods) and neRNAs of interest were quantified in each fraction (Middle box plots). Scale bars top: 0.2 µm, bottom: 1.5 µm. * two-tailed p-value < 0.0001, $n = 3$ biological replicates. (**I**) Top bar graph shows the level of mRNAs of interest in mitochondrial fractions after incubation for 10 min with RNase-A, without RNase A, and with RNase-A + anti-Tom20 antibody in IB buffer, relative to the level of these mRNAs in control mitochondria at baseline. Bottom bar graph shows the level of mRNAs of interest in mitochondrial fractions incubated in IB buffer (Pi: added 10mM inorganic phosphate) relative to the level of these mRNAs in control mitochondria at baseline. Bottom * two-tailed p-value < 0.001, $n = 3$ biological replicates

development [2]. Despite well-documented association of mitochondrial dynamics and neuronal differentiation, a mechanistic basis for the phenomenon remains unclear. Here, we provide evidence that mitochondria drive early dynamics of neuronal differentiation by an unconventional mechanism that involves transient fusion with the nuclear membrane and acquisition of neRNAs. It has been established that a progressive loss of a transcriptional memory (i.e. dominant neRNAs) is an early event during differentiation [6–8]. Transcriptomic remodelling facilitates adoption of a differentiated phenotype by progenitor cells. For example, a loss of neRNAs encoding proteins that propel cell cycle is an early signature of differentiating cells [6]. However, a synchronised reprogramming of genomic, transcriptomic, and metabolomic landscapes of progenitor cells is required to overcome the network resilience [9] of neural progenitor cells that arises from a compensatory feedback between genomic, transcriptomic and metabolomic landscapes. Currently, the mechanism which links and synchronises transcriptomic remodelling to reprogramming of proteomic and metabolomic landscapes remains largely unknown. Here we provide evidence that inter-organellar communication not only alters the transcriptomic and genomic landscapes of neural progenitor cells, but also reprograms the metabolic activity of recipient mitochondria to facilitate emergence of a neuronal profile in an immortalised mouse neural progenitor cell line. These findings are strengthened by evidence for occurrence of inter-organellar communication in developing mouse brain.

Mitochondria acquire neRNAs shortly after induction of neuronal differentiation

An early event that occurred within 0.5 h of inducing neuronal differentiation of C17.2 neural progenitor cells (NPCs) was perinuclear clustering of $Tom20^+$ (Tom20: translocase of outer mitochondrial membrane 20) mitochondria (Fig. 1A, supplementary Fig. S1). These perinuclear mitochondria showed two additional features, an increased transmembrane potential ($\Delta\Psi$) and an expanded inner membrane (Fig. 1B). Parallel to mitochondrial adaptations and within the same timeframe, nuclei of differentiating NPCs showed a partial loss of nuclear envelope protein lamin-B1 (supplementary Fig. S2). While the loss of B-type lamins is a critical driver of differentiation in various cell types [10], coincidence of this organellar adaptation with mitochondrial changes prompted us to question whether these two events are linked. Ultrastructural analysis of perinuclear mitochondria in NPCs at t = 0.5 h after induction of differentiation provided an essential clue. We observed occasional continuity of nuclear and mitochondrial outer membranes in NPCs undergoing differentiation (Fig. 1C). This ultrastructural feature, that was consistent with a transient fusion of the two organelles, was also evident in differentiating neuronal progenitors residing in the subventricular zone of E13 mouse forebrain (C57BL/6 strain) (Fig. 1D). Ultrastructural investigation of differentiating NPCs revealed a further organellar adaptation of mitochondria in a fused state. We observed what appeared to be an extrusion of mitochondrial inner membrane (i.e.

mitoplast) through the fusion pore towards the chromatin (Fig. 1E). In order to study this phenomenon more accurately, we employed live-cell Tau-STED nanoscopy of mitochondria at a high frame rate (2 s/frame) and a photostable mitochondrial inner membrane fluorescent marker, PK Mito Orange (PKMO) [11]. Application of this technology enabled us to dynamically visualise the cycle of extrusion of mitochondrial inner membrane as expansion of $PKMO^{+}$ fine processes along the chromatin at an average rate of ≈400 nm/s followed by retraction towards the origin at approximately the same pace (Fig. 1F, supplementary Movies S1, S2, Fig. S3). Notably, we did not observe any extrusion of mitochondrial inner membrane at T0 prior to induction of differentiation (supplementary Movies S3). A corollary of this phenomenon is that the nuclear matrix and the intermembrane space (IMS) of mitochondria will be in direct communication for seconds during the early stage of neuronal differentiation (Fig. 1E). Application of fluorescence in-situ hybridisation (FISH) afforded a key insight regarding the role of this transient inter-organellar communication in shaping the early differentiation dynamics of NPCs.

Using this methodology, we discovered that β-actin neRNA was strongly colocalized with mitochondrial outer membrane protein Tom20 (a linear signal cross-correlation > 0.4 within a distance of ±60 nm) by t = 0.5 h post-induction of differentiation (Fig. 1G). We then developed a 3D organellar co-incubation method to investigate whether such colocalization is linked to inter-organellar communication that triggers the transfer of neRNAs into mitochondria (Fig. 1H). Using a 3D organellar co-incubation method, isolated mitochondria were mixed with isolated nuclei (ratio: ≈1000 mitochondria/nucleus as per methods) and suspended in a 30μL droplet of RNase-free/protease-free IB buffer (supplemented with 1mM ADP and 1mM pyruvate) for 20 min at 37 °C to maximize interaction of isolated mitochondria and nuclei. After dissociation of the organellar assembly by gentle vibration and differential centrifugation (600 g for 5 min at 4 °C to isolate nuclei and 7000 g for 5 min at 4 °C to isolate mitochondria), organellar RNA was extracted using Trizol reagent, reverse transcribed, and neRNAs of interest were quantified in nuclear and mitochondrial fractions. We noted consistent reduction of β-actin, Ngn1, Ngn2, and Hes-1 mRNAs in the nuclear fraction. Depletion of nuclear neRNAs of interest was concurrent with a ≈2-fold enrichment of mitochondrial neRNAs confirming acquisition of neRNAs by mitochondria (Fig. 1H). In contrast, incubation of the isolated mitochondria with neRNAs in a liquid phase (RNase-free/protease-free IB buffer) did not lead to uptake of these neRNAs by mitochondria (supplementary Fig. S4A). Together, these observations provided preliminary evidence in support of the critical role of inter-organellar communication in direct transfer of neRNAs into mitochondria in our model of early neuronal differentiation. This inference was probed by performing additional experiments.

Mitochondrial acquisition of neRNAs was investigated by employing a nuclease protection assay. Armed with knowledge that mitochondrial Tom20 recognises a generic consensus motif (φχχφφ, φ: hydrophobic and χ: any amino acid) [12], we tested if bovine RNase-A with a characteristic hydrophobic N-terminal sequence of SFLLLLILK (aa1-aa10) can access and degrade β-actin and Hes-1 neRNAs in mitochondria isolated at t = 0.5 h post-induction of differentiation (Fig. 1I). While incubation of the isolated mitochondria with RNase-A in 40 μl of IB buffer for 10 min amplified the baseline degradation rate of β-actin and Hes-1 mRNAs, inhibition of Tom20-mediated mitochondrial transport by application of a specific actibody [13] prevented this activity of RNase-A (Fig. 1I). These findings combined with insights from immunogold labelling of mitochondrial neRNAs (supplementary Fig. S4B) strengthened the inference that the studied neRNAs are within IMS of mitochondria.

Further evidence of the IMS localisation of neRNAs was provided by exploring the baseline degradation of these RNAs. Isolated mitochondria (t = 0.5 h post-induction of differentiation, mitochondrial protein conc. 35 μg/μl) were initially incubated in 40 μl of RNase-free IB buffer supplemented with an RNAse inhibitor (SUPERase•In, 20U) and protease inhibitor cocktail (1 μl). While the IB buffer was determined to be free of ribonuclease activity in control experiments (supplementary Fig. S4C), we noted a time-dependent reduction of the concentration of β-actin and hes-1 mRNAs in isolated mitochondria (Fig. 1I). In the absence of significant ribonuclease activity in the RNase-free IB buffer, our findings suggested that the mitochondria-associated neRNAs are accessible to and degraded by enzymatic activity of mitochondrial IMS RNases. Polynucleotide phosphorylase (PNPase, alias: Pnpt1) and REXO2 are endogenous mitochondrial exonucleases that reside in IMS [14]. PNPase is the main exonuclease that cleaves single-stranded RNA into oligoribonucleotides that are further degraded by REXO2 [15]. We noted that increasing the concentration of inorganic phosphate from 1mM (endogenous) to 10mM amplified the rate of degradation of neRNAs by ≈35% and ≈50% after 5 and 15 min of incubation, respectively (Fig. 1I), characteristic of the phosphate-dependent catalytic activity of PNPase [16]. To validate the role of PNPase in degradation of acquired neRNAs in IMS, we employed RNA interference (RNAi).

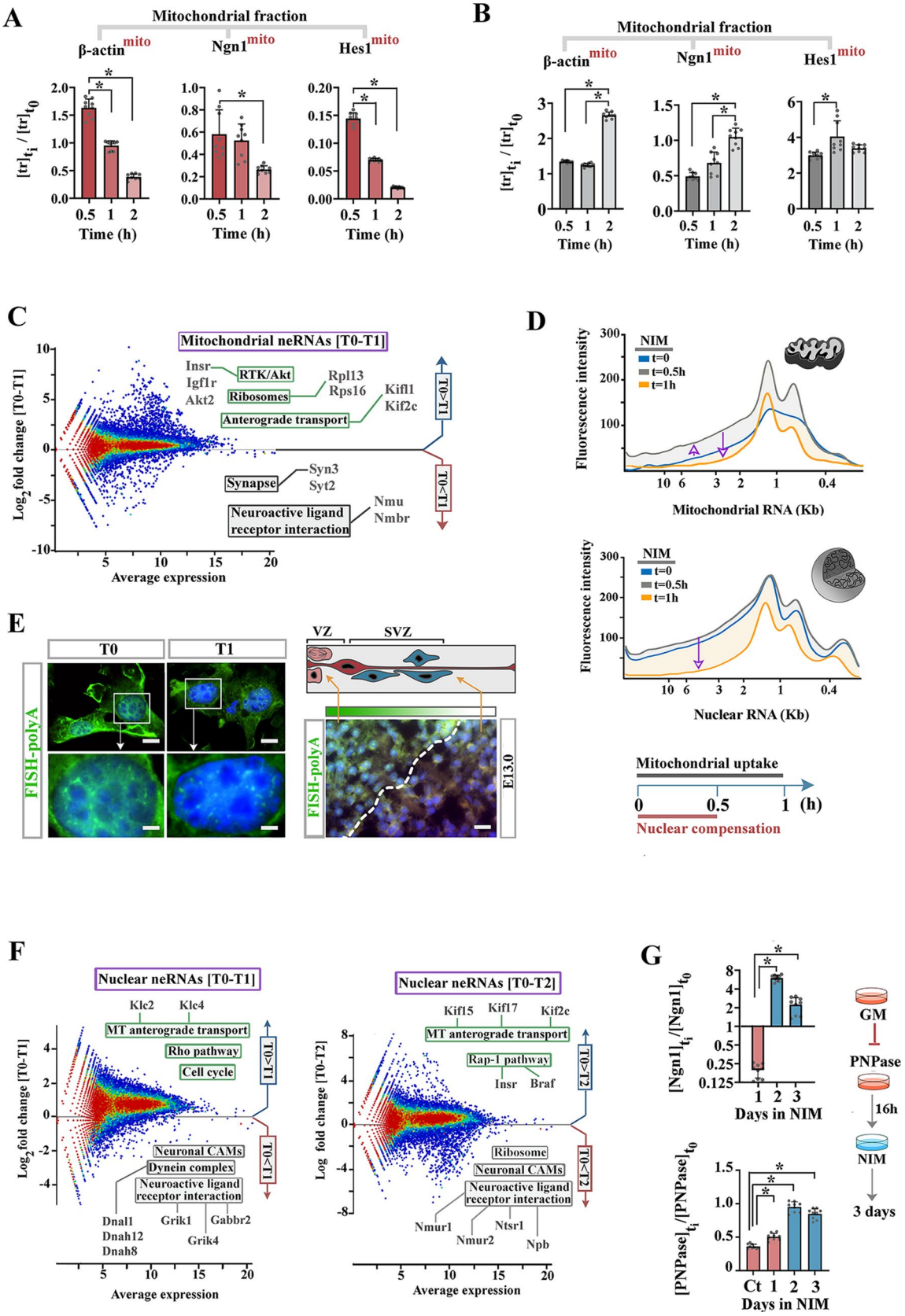

Fig. 2 (See legend on next page.)

(See figure on previous page.)

Fig. 2 Acquisition of neRNAs by mitochondria facilitates emergence of neuronal transcriptome during differentiation. (**A**) Quantification of mRNAs of interest in mitochondrial fractions isolated from differentiating NPCs at different time points (as per the X axis). Values are normalised to levels of the corresponding transcripts in control NPCs at baseline (T0). * two-tailed p-value < 0.0001, error bars: ±1SD, *n* = 3 biological replicates. (**B**) Quantification of mRNAs of interest in mitochondrial fractions isolated from differentiating PNPase^{RNAi} NPCs at different time points (as per the X axis). Values are normalised to levels of the corresponding transcripts in PNPase^{RNAi} NPCs at baseline (T0). * two-tailed p-value < 0.0001, error bars: ±1SD, *n* = 3 biological replicates. (**C**) MA plot shows Log_2 profile of neRNAs acquired by mitochondria isolated from the differentiating cells at t = 1 h relative to mitochondrial neRNAs isolated from the control NPCs (T0). (**D**) Line graphs show the intensity of SYBR Green I dye (y-axis) used in gel electrophoresis of RNAs isolated from mitochondria and nuclei of differentiating NPCs at different time points, plotted against molecular weight of RNAs (x-axis). (**E**) Left photomicrograph shows polyadenylated neRNAs identified using a FISH probe in control (T0) and differentiating (1 h: T1) NPCs *in vitro*. Right micrograph shows polyadenylated neRNAs identified using a FISH probe in ventricular and subventricular zone of a rostral region of E13 mouse neural tube. Note a mosaic pattern of expression characterised by a diminished level of polyA$^+$ neRNAs in the subventricular zone cells. Left scale bars top: 8 µm, bottom: 2 µm. Right scale bar: 30 µm. (**F**) MA plot shows Log_2 profile of neRNAs isolated from the nuclei of differentiating NPCs at t = 1 h and 2 h relative to nuclear neRNAs of the control NPCs (T0). (**G**) Top bar plot shows expression level of Ngn1 in PNPase^{RNAi} differentiating NPCs normalised to control differentiating NPCs. Bottom bar plots demonstrate expression level of PNPase in RNAi^{Pnpt1}-treated versus control NPCs at baseline and after induction of differentiation. * two-tailed p-value < 0.0001, *n* = 3 biological replicates

Mitochondrial acquisition of neRNAs reshapes the transcriptional profile of NPCs

We initially chose three genes from distinct transcriptional categories to study the impacts of inter-organellar communication and PNPase activity on the transcriptional profile of differentiating NPCs: β-actin (steady-state transcription), Hes-1 (expressed in NPCs, repressed upon neuronal differentiation [17, 18]), and Ngn-1 (low expression in NPCs, high expression upon neuronal differentiation). After induction of neuronal differentiation, nuclei and mitochondria were isolated, using a sucrose density gradient, from 2×10^7 NPCs at different time points and the mRNAs of interest were recovered from the organelles and quantified (as detailed in methods). We noted a reduction of the levels of all three studied mRNAs in the mitochondrial fraction isolated from differentiating NPCs at t=0.5 h, 1 h and 2 h post-induction of differentiation (Fig. 2A). The rate of degradation of Hes-1 was the highest amongst the studied mRNAs, whilst Ngn-1 showed the lowest rate of degradation. Application of a cocktail of two siRNAs to target PNPase (PNPase^{RNAi} NPCs) prior to induction of differentiation (post-RNAi incubation period: 16 h) prevented degradation of the studied mRNAs in the mitochondrial fraction isolated from differentiating PNPase^{RNAi} NPCs at all time points (Fig. 2B). The outcome of RNAi experiments confirmed that acquired neRNAs are degraded by nuclease activity of PNPase in IMS. Also, the higher degradation rate of Hes-1 neRNA compared to Ngn-1 neRNA (Fig. 2A) is expected to tip the balance of competition between stemness and neuronal differentiation in favour of the latter, to the extent that findings could be generalised to other neRNAs. In order to probe the generality of this phenomenon, we investigated whether remodelling of the broader transcriptome of NPCs by PNPase-mediated elimination of nuclear neRNAs could contribute to emergence of a pro-neuronal transcriptional profile. The RNA-seq profile of mitochondria at t=1 h was characterised by degradation of a majority of mitochondrial neRNAs present at baseline (Fig. 2C, supplementary Fig. S5). While degradation of transcripts encoding ribosomal proteins could curb the translational capacity of NPCs leading to cell cycle arrest at G1 phase [19], elimination of neRNAs encoding key components of the receptor PI3k/Akt pathway would complement this activity by attenuating the downstream pro-mitogenic signals and enhancing the catabolic flux [20]. Given that key drivers of cell cycle inhibit differentiation dynamics [21], mitochondrial acquisition and degradation of the latter transcripts via PNPase could facilitate neuronal differentiation of NPCs. However, it remained questionable whether the quantity and the rate of acquisition of nuclear neRNAs are high enough to override compensatory transcriptional [22] mechanisms and to alter the profile of neRNAs present within the nucleus.

To answer this question, we isolated mitochondrial and nuclear RNAs from NPCs (2×10^7 cells/time point) at baseline and 0.5 h and 1 h post-induction of differentiation and visualised the isolated RNAs after running a 1% RNase-free agarose gel (Fig. 2D). In the mitochondrial fraction, an increased RNA concentration from t=0 to t=0.5 h was followed by a subsequent reduction of the RNA content at t=1 h (Fig. 2D). Such an oscillation of the RNA content was consistent with acquisition of neRNAs between t=0 and t=0.5 h followed by degradation of the acquired neRNAs between t=0.5 h and t=1 h post-induction of differentiation. In the nuclear fraction, we did not observe a net reduction of neRNA content between t=0 and t=0.5 h post-induction of differentiation despite the uptake of neRNAs by perinuclear mitochondria within the same timeframe (Fig. 2D). This observation could be explained by upregulation of transcription in NPCs at baseline in response to anabolic cues [23] upon exposure to neural induction medium which supplies active metabolites such as insulin and D-glucose, counterbalanced by mitochondrial uptake of nuclear neRNAs. This initial phase of compensation was followed by a marked decline of neRNAs in the nucleus between t=0.5 h and t=1 h after induction of differentiation (Fig. 2D). While such decline of nuclear RNA content could potentially

facilitate a remodelling of the transcriptional profile of NPCs upon differentiation, we asked whether less abundant polyadenylated mRNAs, estimated to comprise ≈ 5% of the total RNA content [24], are sufficiently depleted by inter-organellar communication to alter the composition of nuclear poly(A)$^+$ mRNAs. Identification of poly(A)$^+$ mRNAs by FISH revealed a substantial reduction of polyadenylated neRNAs from the nucleus at t = 1 h after induction of differentiation (Fig. 2E, supplementary Fig. S6). Corroborating the in vitro findings, differentiating neural progenitor cells in the subventricular zone of E13 mouse forebrain exhibited a diminished level of polyadenylated neRNA compared to the proliferating cells of the ventricular zone in the same anatomical region (Fig. 2E, supplementary Fig. S7). Having confirmed that inter-organellar communication along with exonuclease activity of PNPase deplete poly(A)$^+$ mRNAs within the nucleus, we investigated the composition of the emerging nuclear transcriptome of NPCs.

RNA-seq profile of isolated nuclei at t = 1 h post-induction of differentiation was characterised by a depletion of cell cycle-related mRNAs, such as Cdk2 and Cdkn1b, transcripts encoding components of the Rho signalling pathway, such as Tiam2 and Vangl1, and mRNAs encoding proteins that regulate actin cytoskeleton and anterograde transport by microtubules (Fig. 2F). Advancing to t = 2 h post-induction of differentiation, mRNAs related to Rap-1 signalling pathway were also less abundant in the nucleus (Fig. 2F, supplementary Fig. S8). Notably, mRNAs encoding ribosomal proteins were not depleted at t = 1 h despite mitochondrial acquisition of these neRNAs (Fig. 2C). Unaltered levels of ribosomal protein mRNAs is potentially linked to enhanced transcription from these loci (in response to anabolic cues [23]) that stabilised the nuclear neRNA content of NPCs despite significant uptake of neRNAs by mitochondria within 0.5 h of induction of differentiation (Fig. 2D). However, the transcriptional compensation was not ubiquitous and reduced availability of the neRNAs related to cell cycle is expected to facilitate differentiation dynamics [21] of NPCs. Likewise, the decline of mRNAs encoding components of the Rho pathway (Fig. 2C) could potentially contribute to reorganisation of actin cytoskeleton in repurposing the contractile apparatus of migratory NPCs to a molecular platform that supports axon growth and dendrite formation in differentiating NPCs [25]. In parallel, upregulation of neuroactive receptors such as Grik1, Grik4, and Gabbr2 would facilitate emergence of synapses in differentiating neurons [26, 27]. While it appeared that inter-organellar transfer of neRNAs reshapes the composition of the nuclear transcriptome of NPCs towards a neuronal profile, we asked whether this activity is crucial for neuronal differentiation.

To test the assumption that remodelling of the transcriptome of NPCs by mitochondria contributes to neuronal differentiation, we tracked the expression of Ngn1 in PNPase^{RNAi} cells after induction of neuronal differentiation. The level of whole-cell Ngn1 (Ngn1^{Cell}) in PNPase^{RNAi} cells was ≈ 5 fold lower than control differentiating cells at t = 24 h post-differentiation (Fig. 2G). Concurrent with the recovery of PNPase that occurred 48 h after RNAi, we noted ≈ 5.2 fold upregulation of Ngn1 in PNPase^{RNAi} cells relative to control differentiating cells (Fig. 2G). The finding that inhibition of PNPase significantly reduces the differentiation propensity of NPCs in our model system corroborates the reported function of PNPase in driving differentiation dynamics in other model systems [28]. The activity of mitochondrial PNPase in depleting nuclear neRNAs is complemented by simultaneous emergence of neRNAs encoding neuroactive receptors and neuronal cell adhesion molecules, a phenomenon that requires remodelling of chromatin accessibility concurrent with inter-organellar communication.

Mitochondrial acquisition of neRNAs alters higher-order chromatin topology

We employed ATAC-Seq to explore the chromatin accessibility landscape of NPCs upon induction of differentiation. ATAC-seq analysis revealed reduction of chromatin accessibility of promoters belonging to a major genic cluster between t = 0.5 h and t = 1 h post-induction of differentiation (Fig. 3A). The reduced chromatin accessibility that coincided with mitochondrial acquisition and degradation of neRNAs provided a potential explanation for the shut-down of transcriptional compensation between t = 0.5 h to t = 1 h after induction of differentiation (Fig. 2D). Functional analysis of the ATAC-seq profile at t = 1 h post-induction of differentiation revealed that the condensed genic cluster in NPCs included components of the Wnt/β-catenin signalling pathway, such as Wnt5a and Fzd5, and genomic loci that mapped to the PI3k/Akt pathway (Fig. 3A). The de-condensed chromatin, on the other hand, encoded inhibitors of the Wnt pathway such as Kremen-1 and antagonists of the PI3k/Akt pathway such as PTEN (Fig. 3A). The Wnt/β-catenin signalling pathway not only operates as a master-regulator of ribosome biogenesis and global protein synthesis [29] by *trans*-activating Myc [30, 31], but it also inhibits Gsk3β, a pro-catabolic inhibitor of Myc [32]. Therefore, remodelling of the chromatin accessibility landscape complemented the evolving transcriptional profile of NPCs by reducing the accessibility of genomic loci encoding components of pro-anabolic PI3k/Akt and Wnt/β-catenin signalling pathways. Such complementation together with coincidence of inter-organellar communication and chromatin remodelling suggested a link between mitochondrial uptake of nuclear neRNAs and

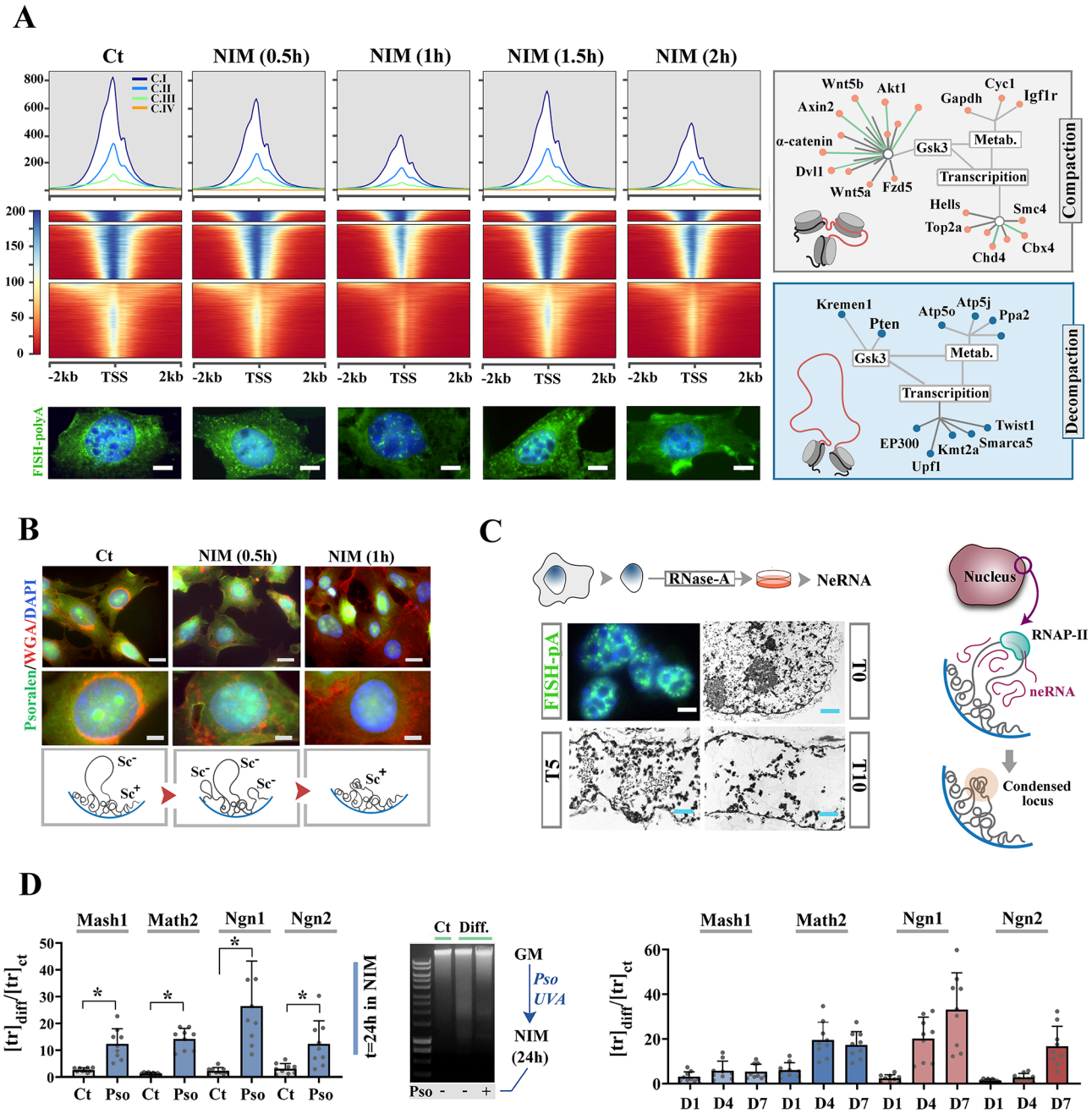

Fig. 3 Efflux of neRNAs alters higher-order chromatin topology. (**A**) Mean signal plots and heatmaps show density of mapped ATAC-seq reads 2 kb up- and downstream of ENSEMBL-annotated transcriptional start sites (TSS) in GRCm39. For every time point ($n=5$ time points), data were partitioned into 4 clusters based on a k-means algorithm. Bottom micrographs show polyadenylated neRNAs identified using a FISH probe in control (T0) and differentiating NPCs in vitro (time points correspond to those of the ATAC-seq profile) (Scale bars: 6 µm). Right panels show global functional mapping of ATAC-seq profile (see methods) into compacted and de-compacted genomic loci in NPCs at t = 1 h after induction of differentiation. (**B**) Micrographs shows the accessible negatively supercoiled chromatin in differentiating NPCs identified by a psoralen probe (see methods). Scale bar top: 10 µm, bottom: 4 µm. Sc^+: positively supercoiled, Sc^-: negatively supercoiled. (**C**) FISH probe shows presence of polyadenylated neRNA in cultured nuclei (t = 20 min) isolated from NPCs (Scale bar: 8 µm). Electron microscopy photomicrographs demonstrate condensation of chromatin after RNAse-A-assisted degradation of neRNAs. Scale bars: 1 µm. (**D**) Application of Psoralen/UVA (Pso^+) to stabilise higher order chromatin topology prior to induction of neuronal differentiation. Expression of pro-neural transcription factors in Pso^+ NPCs 24 h after induction of neuronal differentiation is significantly higher than control NPCs (left graph) and almost equivalent to the level that is achieved in control differentiating NPCs after 7 days (right graph). * two-tailed p-value < 0.0001, $n=3$ biological replicates

alteration of the chromatin accessibility landscape. This potential coupling mechanism was next investigated.

The cyclical nature of chromatin remodelling together with the short periodicity of this event were suggestive of a reversible alteration of higher-order chromatin topology that coincided with mitochondrial uptake of nuclear neRNAs. One such reversible, yet potent mechanism of gene regulation that is highly conserved in various kingdoms of life is regulation of gene accessibility by DNA supercoiling [33, 34] wherein RNA plays a major role via electrostatic interactions [35, 36]. We employed a clickable psoralen probe (Psoralen-TEG azide) to probe the higher-order topology of chromatin in differentiating NPCs. Application of this methodology revealed adoption of a positively supercoiled higher order chromatin topology by NPCs at t=1 h post-induction of differentiation (Fig. 3B, supplementary Fig. S9). Global compaction of DNA in a positively supercoiled (i.e. collapsed) topological state restricts accessibility of chromatin in alignment with the observed global reduction of promoter accessibility of active genes in NPCs at t=1 h (Fig. 3A). Corroborating findings in the culture model, exploration of the subventricular zone of E13 mouse forebrain provided ultrastructural evidence of DNA compaction in differentiating neural progenitor cells (Supplementary Fig. S9). To explore whether chromatin compaction in a positively supercoiled state is triggered by RNA uptake, we treated isolated nuclei with DNase-free RNase-A (conc. 10 µg/mL). Ultrastructural analysis of the isolated nuclei revealed that RNase-A treatment induced condensation of the chromatin within 10 min (Fig. 3C) and corroborated previous reports regarding the structural role of RNA in organising the higher-order topology of chromatin [35, 36]. To validate the proposed role of mitochondria in chromatin remodelling, we co-incubated isolated nuclei and mitochondria which triggered significant depletion of negatively supercoiled (i.e. relaxed) chromatin within 20 min as a consequence of chromatin condensation (Supplementary Fig. S9). We concluded that mitochondrial uptake of neRNAs not only depletes the nuclear neRNAs of NPCs, but it also triggers a collapse of the corresponding genomic loci into a positively supercoiled repressed configuration due to elimination of the neRNAs which are otherwise necessary to keep the loci in an accessible negatively supercoiled state. This inference is bolstered by similarities between the neRNAs depleted at t=1 h (Fig. 2C, F) and the genomic loci that become inaccessible to transposase as assessed by ATAC-seq (e.g. components of the PI3k/Akt pathway) (Fig. 3A).

To validate the role of neRNA-mediated remodelling of the higher-order topology of chromatin in driving differentiation dynamics of NPCs in our model system, we induced inter-strand cross-links in transcriptionally active loci of NPCs using Psoralen/UVA treatment (as per methods) prior to induction of differentiation (Fig. 3D). Psoralen-mediated cross-linking renders the negatively supercoiled DNA transcriptionally inactive [37] mimicking the neRNA-mediated collapse of transcriptionally active loci into an inaccessible positively supercoiled state. In Psoralen-treated NPCs, the enrichment of neRNAs encoding pro-neural transcription factors within 24 h of induction of differentiation was higher than control cells by approximately an order of magnitude and comparable to the level reached in non-treated differentiating cells after 7 days of exposure to differentiation cues (Fig. 3D). Such an acceleration of differentiation dynamics indicated that remodelling of the higher-order topology of chromatin was an essential driver of differentiation dynamics of NPCs. In fact, it can be argued that in the absence of chromatin compaction into a positively supercoiled state, continued compensatory transcription beyond t=0.5 h post-induction of differentiation (Fig. 2D) would have made the transcriptome of NPCs resistant to remodelling. Application of a recombinant RNase-A with a c-Myc nuclear localization signal supported this notion (supplementary Fig. S10). Upon nuclear localisation of the recombinant RNase-A, only a modest reduction of Ngn-1 and β-actin was detected, a resistance that can be attributed to compensatory transcription from the associated loci (supplementary Fig. S10). Thus far, findings portrayed a model of differentiation in our experimental system wherein mitochondrial acquisition and degradation of nuclear neRNAs leads to a transient ablation of genomic memory phased accurately to complement attenuation of the transcriptomic memory of NPCs. A potential caveat for our proposed model of differentiation was that unless the existing proteomic landscape of NPCs is reshaped concurrent with remodelling of transcriptomic and genomic landscapes, the resultant competition could potentially impair differentiation dynamics [38, 39].

Metabolisation of neRNAs reprograms mitochondria

Ultrastructural analysis of NPCs at t=0.5 h and 1 h post-induction of differentiation provided preliminary evidence of proteomic remodelling. We noted existence of large autophagosomes in differentiating NPCs suggesting an amplified autophagic flux (Fig. 4A) that coincided with inter-organellar communication. While there are multiple pathways for induction of autophagy, ATP depletion followed by activation of AMPK pathways are considered as the main inducers of autophagic flux [40].

Exploring the energetic landscape of NPCs following the induction of neuronal differentiation, we detected gradual reduction of the level of ATP in an oscillatory manner over the next 3 h (Fig. 4B). This shift to a negative ATP economy was surprising as the neural induction

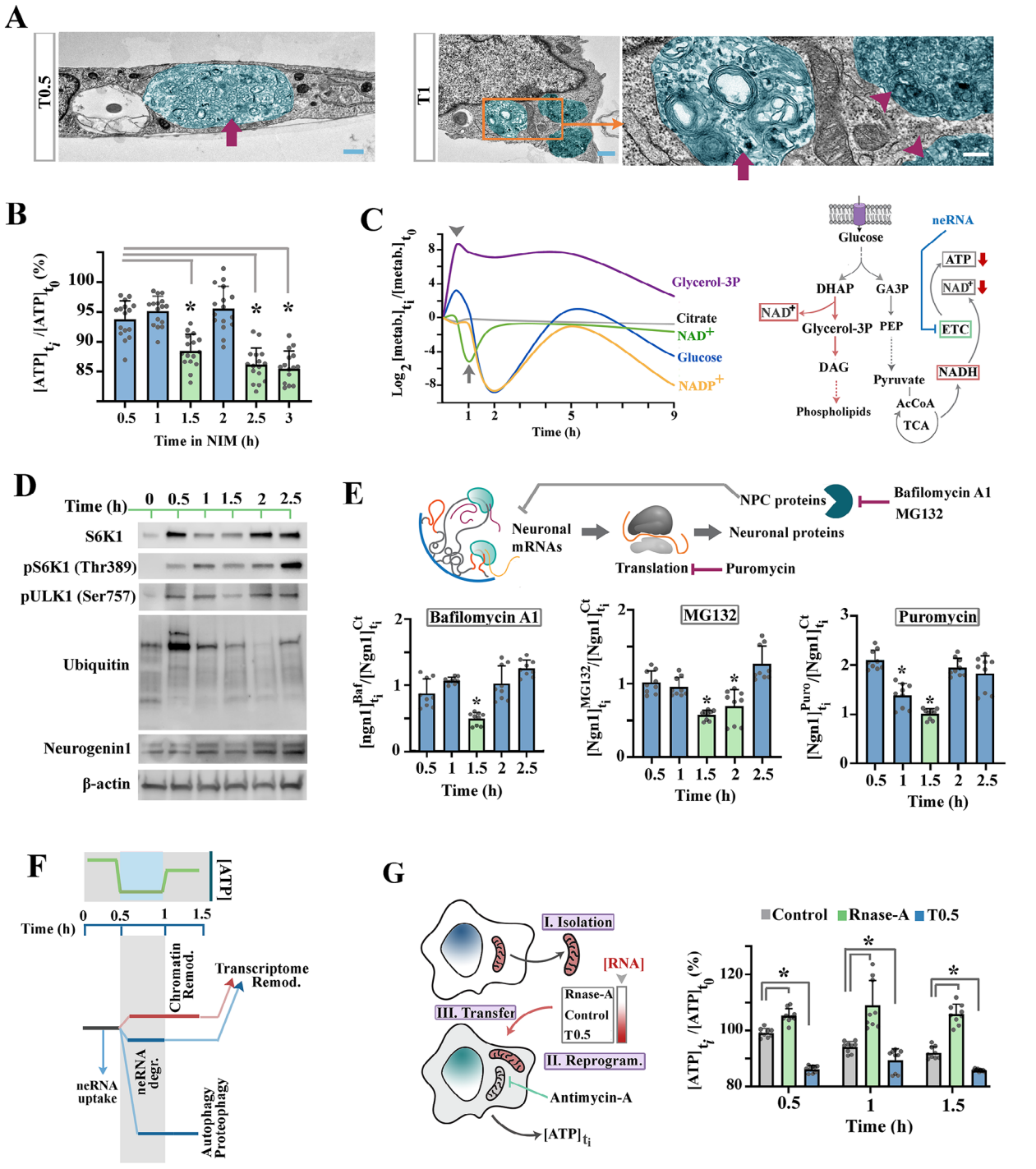

Fig. 4 Acquisition of neRNAs reprograms mitochondrial metabolism. (**A**) Representative electron microscopy photomicrographs of NPCs at t = 0.5 h and 1 h after induction of differentiation. Note the presence of early (arrows) and late (arrowheads) autophagosomes (pseudo-coloured turquoise) in differentiating NPCs. Scale bars left: 2 µm, middle: 1 µm, right: 0.4 µm. (**B**) Graph shows the ATP content of NPCs subsequent to induction of neuronal differentiation. * two-tailed p-value < 0.0001, $n = 3$ biological replicates. (**C**) Graph shows profile of cellular metabolites of central carbon metabolome subsequent to induction of neural differentiation ($n = 1$ sample/time point). Y-axis values represent Log_2 (Area under the curve) for the studied metabolites at different time points during differentiation normalised to Log_2 (Area under the curve) for the metabolites at baseline. (**D**) Western blots show the impact of differentiation on downstream mediators of AMPK and the pro-neural transcription factor Neurogenin-2. (**E**) Bar plot shows expression level of Ngn1 in inhibitor-treated differentiating NPCs normalised to control differentiating NPCs. * two-tailed p-value < 0.0001. (**F**) Schematic demonstration of timeframe of events triggered by inter-organellar communication during differentiation of NPCs. (**G**) Bar plot shows the level of ATP in antimycin-A-treated NPCs receiving isolated and reprogrammed donor mitochondria normalised to the ATP level in antimycin-A-treated recipient NPCs at baseline. * two-tailed p-value < 0.001, $n = 3$ biological replicates

medium provides differentiating cells with 0.12mM iron-bound transferrin, 0.086mM insulin, and 25mM D-glucose, all of which act synergistically to activate the electron transport chain and ATP synthesis [41, 42]. Therefore, we considered an alternative explanation that ATP is potentially reduced due to a high anabolic flux. This alternative explanation, however, appeared to be at odds with the amplified autophagy (Fig. 4A). Hence, in order to gain a deeper insight into the underlying mechanism of ATP reduction, we tracked the temporal profile of central carbon metabolites in differentiating NPCs using LCMS. We noted rapid decline of key metabolites of central carbon metabolism, such as NAD^+, and concurrent elevation of glycerol-3-phosphate (Fig. 4C, supplementary Fig. S11). Conversion of dihydroxyacetone phosphate to glycerol-3-phosphate is a pro-survival metabolic reprogramming that regenerates NAD^+ in cells with a repressed electron transport chain [43]. Accordingly, the level of NAD^+ was restored to the baseline level subsequent to elevation of the level of glycerol-3-phosphate. Together, diminished ATP level, initial depletion of NAD^+, and amplified production of glycerol-3-phosphate strengthened the inference that a repression of the electron transport chain could be responsible for catabolic reprogramming of NPCs and the resultant amplification of autophagic flux.

We then investigated two key downstream mediators of AMP-activated protein kinase (AMPK)/mTOR axis, a pro-survival pathway that induces autophagy upon a shift to a catabolic state. The level of ribosomal protein S6 kinase beta-1 (S6K1), a master-regulator of protein synthesis and cell proliferation, markedly increased from baseline to t=0.5 h which was followed by a significant decline at t=1 h and 1.5 h post-induction of differentiation (Fig. 4D). The enrichment and depletion of S6K1 were in phase with amplification and subsequent degradation of ubiquitinylated proteins (Fig. 4D) suggesting that ubiquitin-mediated selective autophagy [44] could be involved in elimination of S6K1. This possibility was strengthened by the observation that the level of β-actin remained essentially unchanged at all time points, while the level of Ngn-1 increased steadily within the same timeframe (Fig. 4D). Depletion of S6K1 is expected to curb capacity of the translation apparatus [45] in parallel to amplification of selective autophagy that eliminates existing proteins. This period of high autophagic activity was followed by recovery of S6K1 at t=2 h and mTOR-dependent stimulatory phosphorylation of Thr389 of the protein at t=2.5 h, along with inhibitory phosphorylation of Ser757 of Ulk1 to dampen the autophagic flux (Fig. 4D). By comparing the timelines of inter-organellar communication and autophagy, it became apparent that mitochondrial uptake and degradation of nuclear neRNAs at t=1 h (Fig. 2D) and the resultant genomic compaction at t=1 h (Fig. 3A) coincided with the amplified autophagy at t=1 and 1.5 h post-induction of differentiation. We reasoned that alignment of these three events could potentially define a critical window of sensitivity during which the functional memory of stemness at protein level is replaced with a commitment to neuronal differentiation. To test this hypothesis, concurrent with induction of differentiation we applied inhibitors of autophagy (Bafilomycin A1, conc. 20nM) and proteaphagy (MG132, conc.10 μm) 15 min prior to each studied time point followed by washing out of the inhibitors 15 min after the studied time point (see methods) (Fig. 4E). Further, we employed an inhibitor of translation, puromycin (conc. 2 μg/ml), to test the hypothesis that differentiation requires de novo translation of emerging neuronal mRNAs concurrent with autophagic removal of existing proteins of NPCs. By comparing the expression level of Ngn1 over t=16 h in control and treated differentiating NPCs, it became apparent that the critical window of sensitivity of differentiation in our model system occurs between t=1–2 h post-induction of differentiation (Fig. 4E). This is the temporal window during which degradation of nuclear neRNA in IMS, chromatin compaction, and amplified autophagic flux intersected. Given that ATP depletion is critical to AMPK-mediated induction of autophagy, we questioned whether the transition to a catabolic state and the resultant amplification of autophagy are triggered by inter-organellar communication.

To answer this question, mitochondria were isolated from NPCs at baseline (T0) and t=0.5 h after the induction of differentiation (stage I). In stage II of reprogramming, T0.5 mitochondria were split into an untreated group that contained a high load of acquired neRNAs in IMS, and an RNase-A-treated group (incubation time: 20 min) which contained trace amounts of neRNAs in IMS (Fig. 4G). Simultaneously, cultured NPCs (10^5 cells) were treated with 10μM antimycin-A, an inhibitor of cytochrome c reductase, for 30 min to inhibit aerobic respiration in these cells. This compound was selected as unlike other inhibitors of the electron transport chain, antimycin-A does not stimulate a compensatory activation of glycolysis [46]. After ablation of aerobic respiration in cultured NPCs and washing out the inhibitor, the isolated donor mitochondria were transferred into the recipient NPCs in a growth medium via the method of co-incubation [47]. In comparison to NPCs containing the control (T0) donor mitochondria, we observed a consistent reduction of ATP level in cells that received the T0.5 donor mitochondria and the opposite trend of increased ATP level in cells containing the RNase-A-treated donor mitochondria (Fig. 4G). Finding that T0.5 donor mitochondria trigger a reduction of ATP level in the recipient NPCs suggested that these reprogrammed

organelles function as net consumers of ATP [48] within the studied timeframe, thereby driving the transition of NPCs to a catabolic state upon induction of differentiation (Fig. 4B). Next, we incubated NPCs with 25μM Dynarrestin, a small molecule inhibitor of dynein [49], for 30 min prior to induction of differentiation, a treatment that stops microtubule-mediated retrograde migration of mitochondria and the accompanying inter-organellar communication (supplementary Fig. S12A). In contrast to control NPCs, the level of ATP in Dynarrestin-treated NPCs remained high at t=0.5 h and 1 h post-induction of differentiation (supplementary Fig. S12A). Collectively, outcomes of these experiments confirmed that depletion of ATP in differentiating NPCs is a direct consequence of acquisition of nuclear neRNAs. However, the observed transient recovery of ATP level at t=1 h and t=2 h post-induction of differentiation (Fig. 4B) remained unexplained. It can be argued that the transient recovery of ATP in this restricted temporal window is critical as it coincides with PNPase-mediated degradation of default neRNAs of NPCs and emergence of the competing neuronal transcripts, providing an opportunity for enrichment of the proneuronal factors, such as Ngn-1, at protein level (Fig. 4D).

Given that enhanced glycolysis is an adaptive response to a reduction of ATP production by oxidative phosphorylation [46], we wondered whether increased ATP levels at t=1 h and t=2 h post-induction of differentiation (Fig. 4B) is a reflection of enhanced glycolysis rate in response to repressed aerobic respiration. The observation that ATP production remained consistently low in antimycin-A-treated NPCs that received the T0.5 donor mitochondria appeared to be at odds with compensatory upregulation of glycolysis within the studied timeframe (Fig. 4G). Further, pre-incubation of NPCs with 10mM 2-Deoxy-D-glucose (2DG) 2 h prior to induction of differentiation did not completely eliminate fluctuations of the ATP level post-induction of differentiation (supplementary Fig. S12B). Further, ATP production via electron transport chain at t=1 h and t=2 h post-induction of differentiation was an unlikely scenario as the level of glycerol-3-phosphate was high at both time points consistent with a repressed electron transport chain [43]. In support of this line of reasoning, treatment of NPCs with 10μM 2,4-dinitrophenol (an uncoupler of oxidative phosphorylation), did not abolish fluctuations of ATP post-induction of differentiation (supplementary Fig. S12B). We considered an alternative hypothesis that acquired neRNAs not only induce inhibition of electron transport chain (Fig. 4C), but also register a "memory" of the energetic cost of the inhibited state leading to the recovery of ATP production (independent of the electron transport chain) upon PNPase-mediated degradation of neRNAs. This hypothesis was investigated next.

Acquired neRNA mimic an RNA-based metabolic memory of mitochondria

To develop this aspect of the investigation it was necessary to control endogenous mechanisms that regulate ATP synthesis and consumption. Accordingly, mitochondria were isolated at t=0.5 h from differentiating NPCs followed by incubation in EB buffer (containing 2mM Pi, 1mM ADP, and 1mM pyruvate) at 37 °C (Fig. 5A). Under these experimental conditions the excess ADP inhibits ATP hydrolysis [50] leading to a near-linear accumulation of the synthesized ATP, approximating a 0.1% increase in RLU/sec (Fig. 5A). Against this background, rapid and near complete degradation of captured neRNAs by exposure to 1 μl RNase-A resulted in a pulsed production of ATP at a rate that was three orders of magnitude higher than the steady-state rate of ATP synthesis (100% increase in RLU/sec) (Fig. 5A). Replicating the experiment with an ATP/ADP ratio of 2:1 (2mM ATP) resulted in a reversal of synthetic activity of ATP synthase and a gradual reduction of ATP level (Fig. 5B). Even in the hydrolytic state, degradation of mitochondrial neRNAs via RNase-A (1 μl) triggered a pulse of ATP production (Fig. 5B). Such an effective reversal of F_1F_0 ATPase activity from ATP hydrolysis to synthesis is theoretically achievable by an oversupply of ADP or by a sudden amplification of proton motive force (Δp) [48, 50]. As RNA degradation by RNase-A only generates ribonucleoside monophosphate, we suspected that pulsed ATP production could potentially be linked to an increased Δp upon degradation of RNA. To explore this notion, isolated mitochondria were incubated in IB buffer in state 1 (endogenous ADP/pyruvate). While adding 1 μl RNase-A to incubated mitochondria resulted in amplified production of ATP relative to control mitochondria, combined supplementation of ADP (1mM) and RNase-A increased the ATP level by a further ≈70% (Fig. 5C). In contrast, priming the mitochondria with the uncoupler 10μM dinitrophenol (DNP) prior to application of RNase-A resulted in a reduction of ATP production by ≈25% compared to RNase-A treatment only (Fig. 5C). An interpretation of the findings was that the acquired neRNAs reduce Δp by trapping the protons in IMS, an event that is reversed by RNase-A-mediated degradation of neRNAs (Fig. 5D, supplementary Fig. S13). Confirmation of this mechanism was afforded by subsequent experiments whereby incubation of mitochondria (isolated at t=0.5 h) with RNase-A to degrade the acquired neRNAs within IMS led to a reduction of pH both at state 1 (endogenous substrates) and state 3 (added 1mM ADP and 1mM pyruvate) (Fig. 5E). Likewise, RNase-A-mediated degradation of isolated neRNAs brought about a reduction of pH (Fig. 5E). The release of trapped H^+ upon degradation of neRNAs is consistent with a requirement for protonation of RNA upon adopting a secondary structure [51,

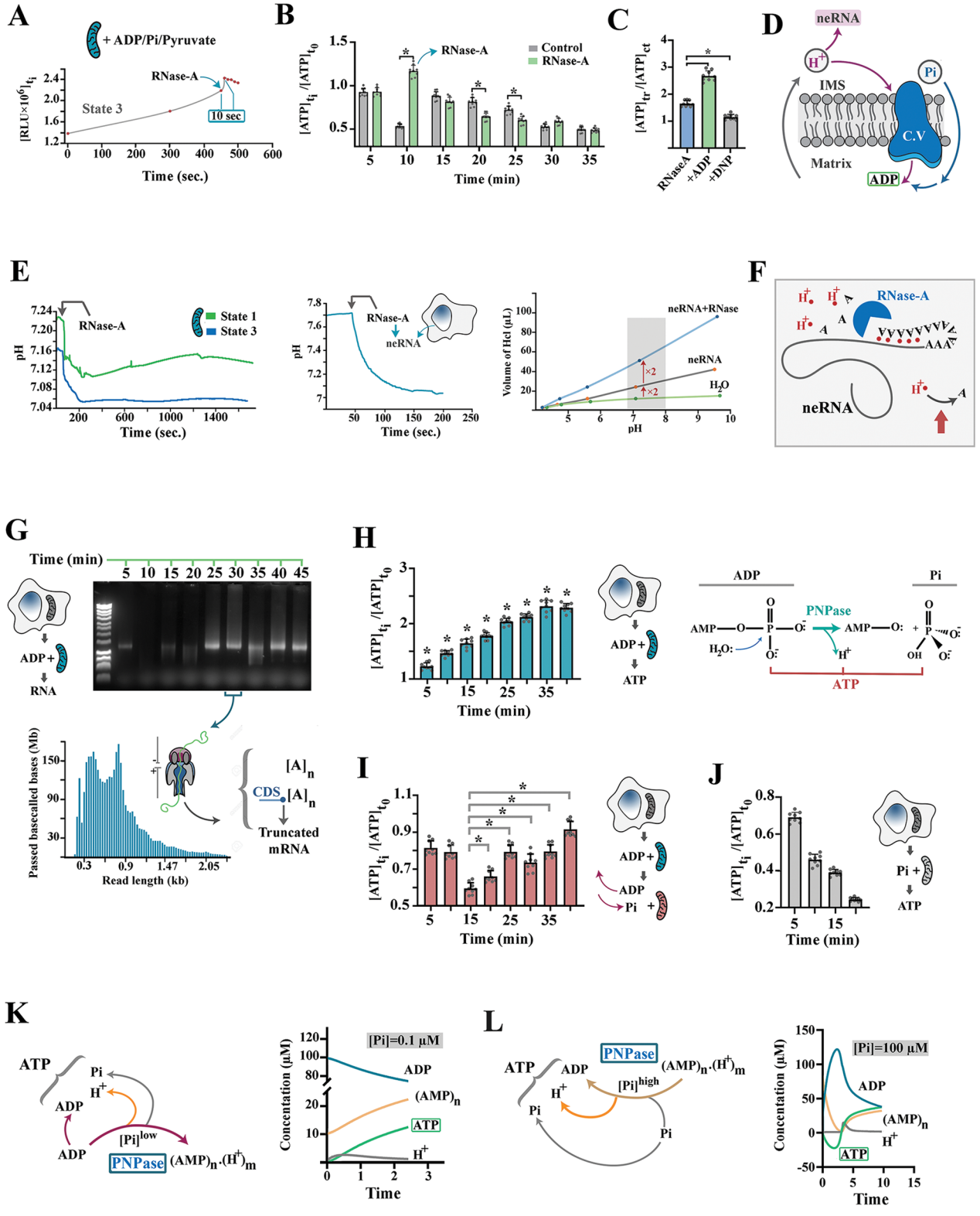

Fig. 5 (See legend on next page.)

(See figure on previous page.)

Fig. 5 NeRNAs reprogram an intrinsic RNA-based memory of mitochondria. (**A**) Graph shows the ATP levels in isolated state-3 mitochondria (supplied with ADP and pyruvate) at different time point prior to and after adding RNase-A. (**B**) Bar graphs show the ATP level of isolated state-3 mitochondria incubated in EB buffer with an ATP: ADP ratio of 2:1 normalised to the ATP content of mitochondria at T0. RNase-A was added at t = 9.5 min. * two-tailed p-value < 0.0001, *n* = 3 biological replicates. (**C**) Bar graphs show the ATP level of isolated state-3 mitochondria incubated in EB buffer after treatment for 10 min with RNase A, RNase-A + ADP, and RNase-A + DNP normalised to the ATP content of mitochondria at T0. * two-tailed p-value < 0.0001, *n* = 3 biological replicates. (**D**) Schematic demonstration of the competition between neRNAs and ATP synthase (complex V) for protons. (**E**) Left and middle graphs show ΔpH after RNase-A treatment of isolated state-1 and state-3 mitochondria (left graph) and RNase-A treatment of isolated nuclear neRNAs (middle graph). Right graph shows titration of 0.025 N HCl against a solution of neRNAs isolated from NPCs at T0 (conc. 150ng/μL) and against a solution of RNase-A-treated neRNAs. (**F**) Schematic demonstration of protons trapped by folded RNA and adenosine monophosphates. (**G**) Gel shows temporal evolution of the RNA content of isolated mitochondria incubated in $IB^{Ca/Mg}$ without access to pyruvate or inorganic Pi and supplied with 1mM adenine. Bar graph shows read depth for RNA sequences of different lengths sequenced using Oxford Nanopore long-read RNA sequencing. Two major signatures of PNPase activity in the isolated RNA pool were poly-A RNAs (i.e. $[A]_n$) generated via primer-independent activity of PNPase and truncated coding sequences flanked by poly-A RNAs (i.e. truncated CDS-$[A]_n$) generated via phosphorolysis of poly-A^+ neRNA which were subsequently used as primers for PNPase to add the poly-A tail (supplementary Data S1, S2). (**H**) Bar graph shows the ATP content of isolated mitochondria incubated in $IB^{Ca/Mg}$ without access to pyruvate or inorganic Pi and supplied with 1mM adenine normalised to the ATP content of mitochondria at T0. * two-tailed p-value < 0.0001, *n* = 3 biological replicates. (**I**) Bar graph shows the ATP content of isolated mitochondria after washing out the ADP and incubating the mitochondria with 2mM Pi in a Ca-free IB buffer (IB^{Mg}) for 10 min normalised to the ATP content of mitochondria at T0. * two-tailed p-value < 0.001, *n* = 3 biological replicates. (**J**) Bar graph shows the ATP content of isolated mitochondria incubated with 2mM Pi in a Ca-free IB buffer (IB^{Mg}) normalised to the ATP content of mitochondria at T0. (**K**) VCell modelling of the proposed mechanism for PNPase-coupled ATP production in a Pi^{Low} condition. Synthetic activity of PNPase is expected to release H^+ and Pi in an equimolar ratio that along with the remaining ADP serve as substrates for ATP synthesis by F_1F_0 synthase. (**L**) Modelling of the proposed mechanism for PNPase-coupled ATP production in a Pi^{High} condition. Phosphorolysis of poly-A RNA by PNPase not only generates ADP but also releases H^+ incorporated into folded RNAs both serving as substrates for ATP synthesis by F_1F_0 synthase

52]. In a following experiment, titration of 0.025 N HCl against a solution of neRNAs isolated from NPCs at T0 (conc. 150ng/μL) indicated that neRNAs function as an organic polymeric proton sump (Fig. 5E), corroborating previous reports regarding the buffering capacity of RNA [53]. Notably, cleavage by-products of neRNAs (nucleoside monophosphates) continued to function as a proton trap (Fig. 5E). Buffering capacity of nucleoside monophosphates was potentially related to pK_{a2} of the terminal phosphate of free ribonucleoside monophosphates (pK_{a2}≈6.0-7.0 [53]) which is exposed after the cleavage of phosphodiester bonds and can trap protons (Fig. 5E). Hence, it was concluded that acquisition of neRNAs assessed at t=0.5 triggers an apparent collapse of Δp by trapping protons (Fig. 5F) leading to a reversal of F_1F_0 ATPase activity from ATP synthesis to hydrolysis (Fig. 4G). Upon phosphorolysis of neRNAs by PNPase activity between t=0.5 h and 1 h, protons trapped by RNA are released, amplifying the Δp, while ADPs generated as by-products of PNPase-mediated phosphorolysis of acquired neRNAs (e.g. poly-A tail of neRNAs) provide the substrate for ATP synthesis.

To validate the proposed mechanism for ATP synthesis by coupling of enzymatic activity of PNPase and F_1F_0 synthase, we focused on the endogenous activity of PNPase. It is known that PNPase drives 5′ → 3′ polymerization of RNA in a low phosphate condition, whereas the enzyme catalyses 3′ → 5′ phosphorolysis of RNA under high phosphate concentration [16]. We explored the energetic consequences of the bimodal activity of PNPase.

To investigate the polymerase activity of PNPase, we reformulated the IB buffer by adding 40mM calcium (IB^{Ca}) to precipitate inorganic phosphate that is released from intracellular sources [54] upon isolation of mitochondria. The remining free calcium was then removed by adding 10mM EGTA. The isolated mitochondria were incubated in a modified IB buffer ($IB^{Ca/Mg}$) containing 10mM $CaCl_2$ (to precipitate Pi generated via the polymerising activity of PNPase), 0.2mM $MgCl_2$ (a cofactor for PNPase [16]) and 1mM ADP (Fig. 5G). Intra-mitochondrial RNA was extracted at 5-minute intervals and visualised after running an agarose gel (Fig. 5G). We noted gradual appearance of a low molecular weight RNA (<500 bp) at t=15 and 20 min post-incubation followed by emergence of higher molecular weight RNAs at t=25 and 30 min. By employing Oxford Nanopore long-read RNA sequencing we were able to reveal the identity of emerging intra-mitochondrial RNAs at t=30 min (Fig. 5G, supplementary Data S1, S2). These were identified as poly-A RNAs synthesized from ADP based on Eq. 1:

$$nADP^{3-} + mH_2O \xrightarrow{PNPase} (AMP^{2-})_m + mH^+ + mHPO_4{}^{2-} + (n-m)ADP^{3-} \quad (1)$$

where ***m*** refers to the number of molecules of adenine polymerised into a poly-A RNA, from an initial pool of ***n*** ADPs, via the activity of PNPase. Analysis of the ATP content of mitochondria at the same time points as in Fig. 5G revealed a surprising facet of the polymerase activity of PNPase; the ATP content of mitochondria incubated in $IB^{Ca/Mg}$ without access to pyruvate (Krebs cycle substrate) or inorganic Pi (a substrate for F_1F_0 synthase) increased in a linear manner (Fig. 5H). A potential mechanism for PNPase-coupled ATP synthesis was that H^+ and Pi released by synthetic activity of PNPase in an equimolar ratio along with the remaining ADP served as

substrates for ATP synthesis by F_1F_0 synthase according to Eq. 2:

$$mH^+ + mHPO_4^{2-} + (n-m)\,ADP^{3-} \xrightarrow{F_1F_0\,Syn.} xATP^{4-} + xH_2O + (n-m-x)\,ADP^{3-} \quad (2)$$

In a synthetic mode (Eq. 1), the inorganic Pi generated via PNPase activity not only serves as a substrate for ATP production; it is expected to prevent excessive build-up of AMP_n (poly-A RNA) in IMS by switching on the 3′ → 5′ exonuclease activity of PNPase, upon exceeding a certain threshold [55]. We explored the impact of the exonuclease activity of PNPase on ATP economy at the same time points as in Fig. 5G by washing out the ADP and incubating the mitochondria in 2mM Pi in a Ca-free IB buffer (IB^{Mg}) for 10 min (Fig. 5I). Despite an initial reduction at t=15 min, the ATP content of mitochondria incubated in IB^{Mg} (no pyruvate/ADP) returned to pre-incubation level after t=40 min (Fig. 5I). The initial reduction of ATP content was presumably due to the removal of ADP triggering the default hydrolytic activity of F_1F_0 synthase (Fig. 5J). Following this initial hydrolysis, the ATP content rose steadily after t=15 min. Once again, accumulation of ATP can be explained by exonuclease activity of PNPase that not only generates ADP via phosphorolysis of poly-A RNA but also releases H^+ incorporated into folded RNAs (Fig. 5E) according to Eq. 3:

$$(AMP^-)_m.zH^+ + mHPO_4^{2-} \xrightarrow{PNPase} mADP^{3-} + zH^+ \quad (3)$$

where $\mathbf{z}H^+$ refers to protons trapped in folded RNAs (Fig. 5E). The structurally trapped protons, ADP, and Pi (a component of IB^{Mg} buffer) provide the necessary substrates for synthesis of ATP by F_1F_0 synthase independent of the electron transport chain according to Eq. 4:

$$zH^+ + zHPO_4^{2-} + mADP^{3-} \xrightarrow{F_1F_0\,Syn.} zATP^{4-} + (m-z)\,ADP^{3-} \quad (4)$$

We used VCell software to model the suggested mechanism for PNPase-coupled production of ATP based on Eqs. 1–4 (Fig. 5K, L, for details of the model refer to Methods). The output of VCell modelling corroborated the experimental results foreshadowing a biphasic mitochondrial back-up metabolism whereby synthesis of AMP_n from ADP upon nutrient starvation leads to generation of ATP and release of Pi (Fig. 5K). The released Pi provides negative feedback to PNPase switching on the exonuclease activity of PNPase triggering degradation of RNAs stored in IMS and releasing ADP and H^+ that serve as substrates for F_1F_0 synthase (Fig. 5L).

Demonstration of an RNA-based ATP economy that operates by coupling of PNPase to F_1F_0 synthase provided a mechanistic rationale for neRNA-mediated reprogramming of mitochondrial ATP production. Acquired neRNAs mimic RNAs synthesized by PNPase, with two major differences. Krebs cycle by-products such as citrate inhibit the enzymatic activity of PNPase [56], restricting IMS-intrinsic RNA synthesis by PNPase to periods of inactive electron transport chain (i.e. nutrient starvation) preventing a collapse of the proton motive force. Also, while excessive accumulation of endogenous poly-A RNAs in the mitochondrial backup metabolism is prevented due to demonstrated Pi-mediated negative feedback, there seems to be no such mechanism to restrict the uptake of neRNAs by inter-organellar communication. Therefore, acquired neRNAs initially inhibit ATP production by trapping protons leading to a collapse of proton motive force (at t=0.5 h in our model system) and a resultant amplification of autophagic flux. Subsequent degradation of neRNAs by PNPase (Fig. 2D) leads to a pulsatile synthesis of ATP upon differentiation (at t=1 h in our model system) in a manner analogous to removal of IMS-intrinsic RNAs by exonuclease activity of this enzyme. Hence, it appears that acquired neRNAs reprogram mitochondrial metabolism by hijacking the RNA-based ATP economy of the organelle aligning the metabolic landscape to the remodelled transcriptomic and genomic landscapes of differentiating NPCs (Fig. 6).

Discussion

Our findings add a mechanistic twist to the existing knowledge regarding the central role of mitochondria in driving neuronal differentiation [1–5]. Mitochondria appear to accommodate two mutually exclusive operational modes, an explicit bioenergetic mode and an implicit transcriptome remodelling mode. In the transcriptome remodelling mode, mitochondrial acquisition and degradation of neRNAs curbs the transcriptomic memory of progenitor cells, while simultaneously suppressing ATP production, and inducing chromatin condensation. Such synchronised reprogramming of genomic, transcriptomic, and metabolomic landscapes facilitates differentiation by overcoming the network resilience [9] of neural progenitor cells that would otherwise pose a significant challenge to differentiation due to compensatory feedback between genomic, transcriptomic and metabolomic landscapes.

The described mechanism for mitochondria-mediated induction of neural differentiation is supported by extant literature at multiple levels. There is emerging evidence for transfer of nuclear-encoded RNAs into mitochondria [57–59]. In an analysis of mitochondrial transcriptome, Mercer et al. were surprised to discover that 86% of the mitochondrial transcriptome consists of nuclear encoded RNAs [60]. The authors attributed this finding to the presence of membrane-associated neRNAs [60].

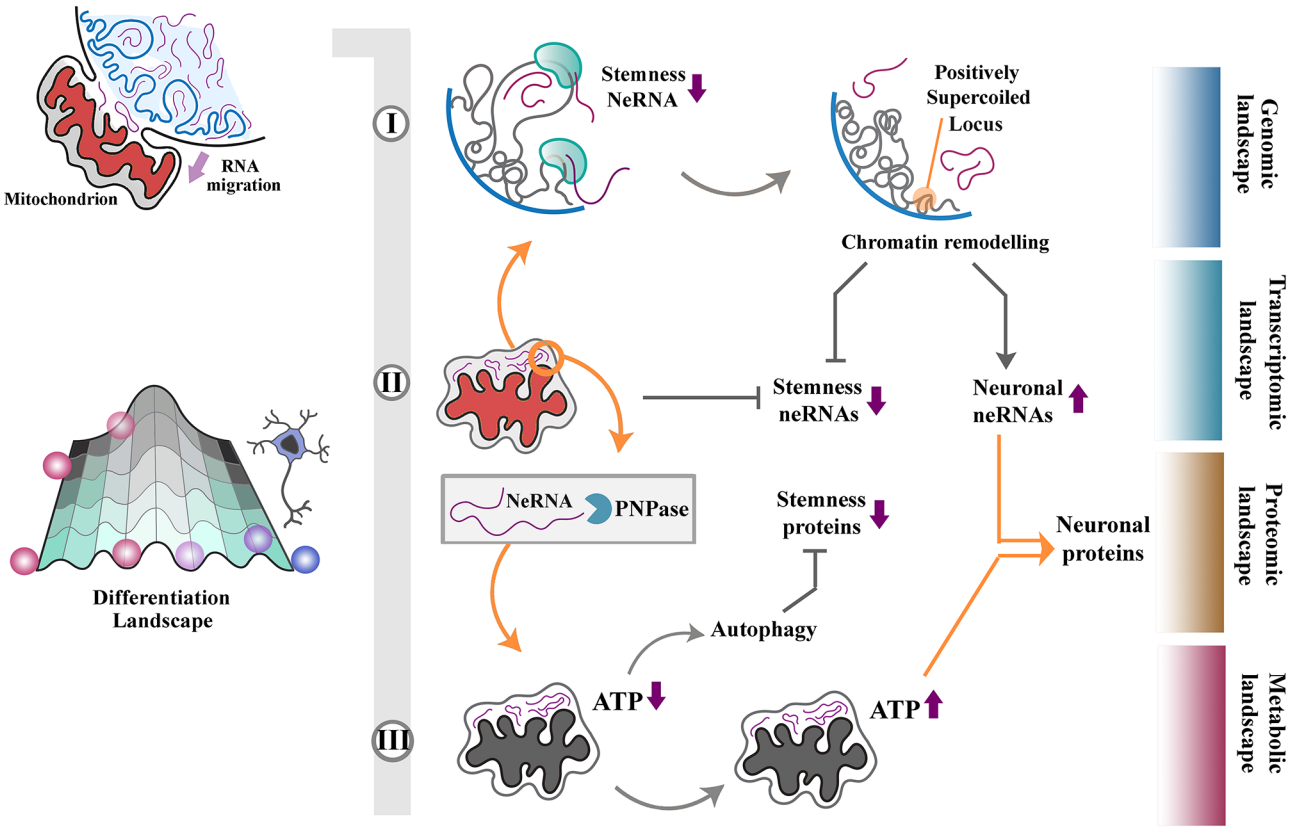

Fig. 6 Schematic demonstration of the proposed role of mitochondria in driving neuronal differentiation by inter-organellar communication. Acquisition and degradation of neRNAs by mitochondria tips the balance of competition between stemness and neuronal neRNAs in favor of neuronal neRNAs. Adoption of a positively supercoiled state by chromatin complements depletion of stemness neRNAs by inter-organellar communication. Synchronised neRNA-mediated metabolic reprogramming of mitochondria induces autophagy and aligns the proteomic landscape to the altered transcriptomic and genomic profiles of differentiating NPCs. Such synchronised reprogramming of genomic, transcriptomic, and metabolomic landscapes facilitates differentiation through eliminating a network resilience barrier that is enforced by compensatory feedback between genomic, transcriptomic and metabolomic landscapes

However, the presence of 5 S rRNA in highly purified mitochondrial fractions of human and rat cells suggests that mitochondrial neRNAs are authentic organellar species imported by an unknown mechanism into mitochondria [61]. A similar conclusion was reached by Puranam et al. who noted the presence of H1 RNA within mitochondria [62]. Our findings suggest a mechanism whereby neRNAs can be imported into mitochondrial IMS via transient inter-organellar fusion during induction of differentiation. The evidence for transient fusion between mitochondria and nuclei in a homeostatic state corroborates our findings that inter-organellar communication functions as an neRNA transfer mechanism into mitochondria [63].

Central to inter-organellar communication is fusion of the mitochondrial outer membrane with the nuclear membrane that establishes a direct communication channel between these two organelles. Subsequent migration of neRNAs into mitochondria could potentially be driven by electrophoretic mobility of negatively charged neRNAs towards the positively charged mitoplast which transiently extrudes into the nucleus. The transmembrane potential ($\Delta\Psi_M$) of State-4 mitochondria is estimated as +180 mV [64], generated by H^+ ions that are trapped on the outer surface of inner mitochondrial membrane lipids [65, 66]. Conversely, the major groove of a phosphate-rich RNA helix has an average negative potential of -400 mV, and the minor groove is estimated to have a negative potential of -200 mV [67]. Given a conservative estimate of a distance of 200 nm between the IMS and nuclear neRNAs during inter-organellar fusion, this event could generate an estimated voltage gradient of 10 kV/cm capable of mobilising typical eukaryotic neRNAs from the nucleus into the IMS. Despite theoretical plausibility of the proposed mechanism, further research is needed to explore whether electrostatic interactions underpin acquisition of neRNAs by mitochondria. Regardless of the exact mechanism for capturing neRNAs, the process is expected to be facilitated by the observed expansion of mitoplast beyond the fusion pore which increases the available surface areas for trapping neRNAs within the restricted temporal window (seconds) of inter-organellar

communication. While details of molecular mechanisms that underpin expansion of mitochondrial inner membrane, as a prerequisite for extrusion of mitoplast, have been reviewed elsewhere [68], there seems to a be a direct link between mitochondrial energetics and morphology. ATP synthase, for example, plays a structural role in supporting expansion of mitochondrial crista [69]. Also, enrichment of positively charged cardiolipin is required for sustaining the negative curvature of crista upon expansion of mitochondrial inner membrane [70]. One could argue that concordance of factors that enhance density of membrane-tethered positive charges and the surface area of mitochondrial inner membrane enhance the potential for capturing nuclear neRNAs by inter-organellar communication.

Efficiency of inter-organellar communication in driving neuronal differentiation stems from the unique enzymatic behaviour of PNPase both in exonuclease and polymerising modes. In exonuclease mode, PNPase operates by phosphorolysis generating ribonucleoside diphosphates unlike hydrolytic activity of other RNAses that leads to production of ribonucleoside monophosphates [16]. ADP, a by-product of phosphorolysis of RNA, is utilised in ATP synthesis subsequent to PNPase-mediated degradation of neRNAs. In consequence, PNPase-mediated depletion of stemness-related neRNAs triggers two events in a synchronised manner; expression of competing neuronal neRNAs and ATP production. Along with depletion of stemness-related neRNAs, enrichment of neuronal neRNAs in an ATP-rich environment that empowers the translation apparatus, force progenitor cells towards a "tipping point" characterised by emergence of a competing neuronal differentiation program at the protein level. While under experimental conditions of our model system, such tipping point occurs within a temporal window between t=1–2 h post-induction of differentiation, it remains to be determined whether differentiation in vivo follows a similar path or that NPCs traverse multiple such tipping points prior to embarking on neuronal differentiation.

Limitations and methodological challenges

A key limitation of the current study is that despite some preliminary evidence of generality [28], the extent of contribution of inter-organellar communication to differentiation in other cell lineages remains unknown. While we provide in vivo evidence for occurrence of inter-organellar communication in developing mouse brain, subsequent experiments were all performed using an immortalized mouse neural progenitor cell line. Hence, the documented role of mitochondria as "reprogrammers" of differentiation remains to be validated in other neuronal lineages and in vivo.

Aside from in vivo observations, two corroborating circumstantial lines of evidence regarding the role of PNPase in differentiation provide preliminary indication that the proposed mechanism is not confined to the studied cell model. Leszczyniecka observed significant upregulation of PNPase in differentiating cells concomitant with a global RNA degradation in an in vitro model [28]. Further, it has been reported that mutations in the gene encoding the human PNPase that reduce its activity lead to hereditary hearing loss, encephalomyopathy, severe axonal neuropathy, delayed myelination, and Leigh syndrome [71, 72]. Given the critical role of PNPase in regulating mitochondrial function [73], a deeper analysis of inter-organellar communication will require significant methodological innovations to study the role of PNPase in this process without affecting mitochondrial function.

In summary, we provide evidence for a transient fusion event between mitochondria and nucleus that leads to efflux of neRNAs into mitochondrial IMS. Degradation of the acquired neRNAs results in reprogramming of mitochondrial metabolic activity along with transcriptomic and genomic remodelling of neural progenitor cells. Mitochondrial mediated synchronised reprogramming of metabolomic, transcriptomic, and genomic profiles facilitates neural differentiation of progenitor cells.

Supplementary Information

The online version contains supplementary material available at https://doi.org/10.1186/s12964-024-01825-1.

Supplementary Material 1

Supplementary Material 2

Supplementary Material 3

Supplementary Material 4

Supplementary Material 5

Supplementary Material 6

Acknowledgements

Not applicable.

Author contributions

Conceptualization: RMFMethodology: RMF, NH, WEH, MS, CES.Investigation: RMF, FV WEH.Visualization: RMF, WEH.Funding acquisition: RMF, NH. Project administration: RMF.Data interpretation: RMF, NH, CES, FV. Supervision: RMF, NH. Writing – original draft: RMF.Writing – review & editing: FV, MS, WEH, CES, NH, RMF.

Funding

This work was supported by internal funding.

Data availability

No datasets were generated or analysed during the current study.

Declarations

Competing interests

The authors declare no competing interests.

Received: 6 July 2024 / Accepted: 11 September 2024
Published online: 26 September 2024

References

1. Iwata R, Casimir P, Vanderhaeghen P. Mitochondrial dynamics in postmitotic cells regulate neurogenesis. Science. 2020;369:858–62. https://doi.org/10.1126/science.aba9760.
2. Ozsoy S, et al. Cannibalized erythroblasts accelerate developmental neurogenesis by regulating mitochondrial dynamics. Cell Rep. 2021;35:108942. https://doi.org/10.1016/j.celrep.2021.108942.
3. Beckervordersandforth R et al. Role of Mitochondrial Metabolism in the Control of Early Lineage Progression and Aging Phenotypes in Adult Hippocampal Neurogenesis. *Neuron* 93, 560–573 e566, https://doi.org/10.1016/j.neuron.2016.12.017 (2017).
4. Khacho M, et al. Mitochondrial dynamics impacts Stem Cell Identity and Fate decisions by regulating a Nuclear Transcriptional Program. Cell Stem Cell. 2016;19:232–47. https://doi.org/10.1016/j.stem.2016.04.015.
5. Khacho M, Slack RS. Mitochondrial dynamics in the regulation of neurogenesis: from development to the adult brain. Dev Dyn. 2018;247:47–53. https://doi.org/10.1002/dvdy.24538.
6. Fourneaux C et al. Differentiation is accompanied by a progressive loss in transcriptional memory. *Bmc Biol* 22, ARTN 58 https://doi.org/10.1186/s12915-024-01846-9 (2024).
7. Samuels TJ, Gui J, Gebert D. Karam Teixeira, F. two distinct waves of transcriptome and translatome changes drive Drosophila germline stem cell differentiation. EMBO J. 2024;43:1591–617. https://doi.org/10.1038/s44318-024-00070-z.
8. Wu JQ, et al. Dynamic transcriptomes during neural differentiation of human embryonic stem cells revealed by short, long, and paired-end sequencing. P Natl Acad Sci USA. 2010;107:5254–9. https://doi.org/10.1073/pnas.0914114107.
9. Wagner A. Robustness and evolvability: a paradox resolved. Proc Biol Sci. 2008;275:91–100. https://doi.org/10.1098/rspb.2007.1137.
10. Solovei I, et al. LBR and lamin A/C sequentially tether peripheral heterochromatin and inversely regulate differentiation. Cell. 2013;152:584–98. https://doi.org/10.1016/j.cell.2013.01.009.
11. Liu T, et al. Multi-color live-cell STED nanoscopy of mitochondria with a gentle inner membrane stain. Proc Natl Acad Sci U S A. 2022;119:e2215799119. https://doi.org/10.1073/pnas.2215799119.
12. Saitoh T, et al. Tom20 recognizes mitochondrial presequences through dynamic equilibrium among multiple bound states. EMBO J. 2007;26:4777–87. https://doi.org/10.1038/sj.emboj.7601888.
13. Grey JY, et al. Tom20-mediated mitochondrial protein import in muscle cells during differentiation. Am J Physiol Cell Physiol. 2000;279:C1393–1400. https://doi.org/10.1152/ajpcell.2000.279.5.C1393.
14. Bruni F, Lightowlers RN, Chrzanowska-Lightowlers ZM. Human mitochondrial nucleases. FEBS J. 2017;284:1767–77. https://doi.org/10.1111/febs.13981.
15. Szewczyk M, et al. Human REXO2 controls short mitochondrial RNAs generated by mtRNA processing and decay machinery to prevent accumulation of double-stranded RNA. Nucleic Acids Res. 2020;48:5572–90. https://doi.org/10.1093/nar/gkaa302.
16. Littauer UZ, Soreq H. in *The Enzymes* (ed P.D. Boyer) Ch. 17, 517–553Academic Press, (1982).
17. Nakamura Y, et al. The bHLH gene hes1 as a repressor of the neuronal commitment of CNS stem cells. J Neurosci. 2000;20:283–93. https://doi.org/10.1523/JNEUROSCI.20-01-00283.2000.
18. Ohtsuka T, et al. Hes1 and Hes5 as notch effectors in mammalian neuronal differentiation. EMBO J. 1999;18:2196–207. https://doi.org/10.1093/emboj/18.8.2196.
19. Bernstein KA, Bleichert F, Bean JM, Cross FR, Baserga SJ. Ribosome biogenesis is sensed at the start cell cycle checkpoint. Mol Biol Cell. 2007;18:953–64. https://doi.org/10.1091/mbc.E06-06-0512.
20. Manning BD, Toker AAKTPKB, Signaling. Navigating the network. Cell. 2017;169:381–405. https://doi.org/10.1016/j.cell.2017.04.001.
21. Ruijtenberg S, van den Heuvel S. Coordinating cell proliferation and differentiation: antagonism between cell cycle regulators and cell type-specific gene expression. Cell Cycle. 2016;15:196–212. https://doi.org/10.1080/15384101.2015.1120925.
22. Rossi A, et al. Genetic compensation induced by deleterious mutations but not gene knockdowns. Nature. 2015;524:230–3. https://doi.org/10.1038/nature14580.
23. Martin D, Soulard E, Hall A, N M. TOR regulates ribosomal protein gene expression via PKA and the Forkhead transcription factor FHL1. Cell. 2004;119:969–79. https://doi.org/10.1016/j.cell.2004.11.047.
24. Yi H, et al. Duplex-specific nuclease efficiently removes rRNA for prokaryotic RNA-seq. Nucleic Acids Res. 2011;39:e140. https://doi.org/10.1093/nar/gkr617.
25. Hall A, Lalli G. Rho and Ras GTPases in axon growth, guidance, and branching. Cold Spring Harb Perspect Biol. 2010;2:a001818. https://doi.org/10.1101/cshperspect.a001818.
26. Oh WC, Lutzu S, Castillo PE, Kwon HB. De novo synaptogenesis induced by GABA in the developing mouse cortex. Science. 2016;353:1037–40. https://doi.org/10.1126/science.aaf5206.
27. Rasse TM, et al. Glutamate receptor dynamics organizing synapse formation in vivo. Nat Neurosci. 2005;8:898–905. https://doi.org/10.1038/nn1484.
28. Leszczyniecka M, et al. Identification and cloning of human polynucleotide phosphorylase, hPNPase old-35, in the context of terminal differentiation and cellular senescence. Proc Natl Acad Sci U S A. 2002;99:16636–41. https://doi.org/10.1073/pnas.252643699.
29. Grandori C, et al. c-Myc binds to human ribosomal DNA and stimulates transcription of rRNA genes by RNA polymerase I. Nat Cell Biol. 2005;7:311–8. https://doi.org/10.1038/ncb1224.
30. He TC, et al. Identification of c-MYC as a target of the APC pathway. Science. 1998;281:1509–12. https://doi.org/10.1126/science.281.5382.1509.
31. Herbst A, et al. Comprehensive analysis of beta-catenin target genes in colorectal carcinoma cell lines with deregulated Wnt/beta-catenin signaling. BMC Genomics. 2014;15:74. https://doi.org/10.1186/1471-2164-15-74.
32. Jellusova J, et al. Gsk3 is a metabolic checkpoint regulator in B cells. Nat Immunol. 2017;18:303–12. https://doi.org/10.1038/ni.3664.
33. Martis BS, Forquet R, Reverchon S, Nasser W, Meyer S. DNA supercoiling: an Ancestral Regulator of Gene expression in pathogenic Bacteria? Comput Struct Biotechnol J. 2019;17:1047–55. https://doi.org/10.1016/j.csbj.2019.07.013.
34. Rezaei-Lotfi S, Vujovic F, Simonian M, Hunter N, Farahani RM. Programmed genomic instability regulates neural transdifferentiation of human brain microvascular pericytes. Genome Biol. 2021;22:334. https://doi.org/10.1186/s13059-021-02555-0.
35. Nickerson JA, Krochmalnic G, Wan KM, Penman S. Chromatin architecture and nuclear RNA. Proc Natl Acad Sci U S A. 1989;86:177–81. https://doi.org/10.1073/pnas.86.1.177.
36. Maison C, et al. Higher-order structure in pericentric heterochromatin involves a distinct pattern of histone modification and an RNA component. Nat Genet. 2002;30:329–34. https://doi.org/10.1038/ng843.
37. Shi YB, Gamper H, Vanhouten B, Hearst JE. Interaction of Escherichia-Coli Rna-Polymerase with DNA in an Elongation Complex arrested at a specific psoralen Crosslink Site. J Mol Biol. 1988;199:277–93. https://doi.org/10.1016/0022-2836(88)90314-2.
38. Tsukamoto S, et al. Autophagy is essential for preimplantation development of mouse embryos. Science. 2008;321:117–20. https://doi.org/10.1126/science.1154822.
39. Mizushima N, Levine B. Autophagy in mammalian development and differentiation. Nat Cell Biol. 2010;12:823–30. https://doi.org/10.1038/ncb0910-823.
40. Singh R, Cuervo AM. Autophagy in the cellular energetic balance. Cell Metab. 2011;13:495–504. https://doi.org/10.1016/j.cmet.2011.04.004.
41. Cheng Z, Tseng Y, White MF. Insulin signaling meets mitochondria in metabolism. Trends Endocrinol Metab. 2010;21:589–98. https://doi.org/10.1016/j.tem.2010.06.005.
42. Ward DM, Cloonan SM. Mitochondrial Iron in Human Health and Disease. Annu Rev Physiol. 2019;81:453–82. https://doi.org/10.1146/annurev-physiol-020518-114742.
43. Liu S et al. Glycerol-3-phosphate biosynthesis regenerates cytosolic NAD(+) to alleviate mitochondrial disease. *Cell Metab* 33, 1974–1987 e1979, https://doi.org/10.1016/j.cmet.2021.06.013 (2021).
44. Kraft C, Peter M, Hofmann K. Selective autophagy: ubiquitin-mediated recognition and beyond. Nat Cell Biol. 2010;12:836–41. https://doi.org/10.1038/ncb0910-836.
45. Holz MK, Ballif BA, Gygi SP, Blenis J, mTOR. S6K1 mediate assembly of the translation preinitiation complex through dynamic protein interchange and ordered phosphorylation events. Cell. 2021;184:2255. https://doi.org/10.1016/j.cell.2021.03.060.

46. Dickman KG, Mandel LJ. Differential effects of respiratory inhibitors on glycolysis in proximal tubules. Am J Physiol. 1990;258:F1608–1615. https://doi.org/10.1152/ajprenal.1990.258.6.F1608.
47. Clark MA, Shay JW. Mitochondrial transformation of mammalian cells. Nature. 1982;295:605–7. https://doi.org/10.1038/295605a0.
48. Valdebenito GE, Chacko AR, Duchen MR. The mitochondrial ATP synthase as an ATP consumer-a surprising therapeutic target. EMBO J. 2023. https://doi.org/10.15252/embj.2023114141.
49. Hoing S et al. Dynarrestin, a Novel Inhibitor of Cytoplasmic Dynein. *Cell Chem Biol* 25, 357–369 e356, https://doi.org/10.1016/j.chembiol.2017.12.014 (2018).
50. Vinogradov AD. Steady-state and pre-steady-state kinetics of the mitochondrial F1F0 ATPase:: is ATP synthase a reversible molecular machine? J Exp Biol. 2000;203:41–9.
51. Moody EM, Lecomte JT, Bevilacqua PC. Linkage between proton binding and folding in RNA: a thermodynamic framework and its experimental application for investigating pKa shifting. *RNA* 11, 157–172, https://doi.org/10.1261/rna.7177505 (2005).
52. Faison EM, Nallathambi A, Zhang Q. Characterizing protonation-coupled conformational ensembles in RNA via pH-Differential Mutational profiling with DMS probing. J Am Chem Soc. 2023;145:18773–7. https://doi.org/10.1021/jacs.3c07736.
53. Thaplyal P, Bevilacqua PC. Experimental approaches for measuring Pka's in RNA and DNA. Methods Enzymol. 2014;549:189–219. https://doi.org/10.1016/B978-0-12-801122-5.00009-X.
54. Bevington A, et al. A study of intracellular orthophosphate concentration in human muscle and erythrocytes by 31P nuclear magnetic resonance spectroscopy and selective chemical assay. Clin Sci (Lond). 1986;71:729–35. https://doi.org/10.1042/cs0710729.
55. Portnoy V, Palnizky G, Yehudai-Resheff S, Glaser F, Schuster G. Analysis of the human polynucleotide phosphorylase (PNPase) reveals differences in RNA binding and response to phosphate compared to its bacterial and chloroplast counterparts. RNA. 2008;14:297–309. https://doi.org/10.1261/rna.698108.
56. Stone CM, et al. Inhibition of homologous phosphorolytic ribonucleases by citrate may represent an evolutionarily conserved communicative link between RNA degradation and central metabolism. Nucleic Acids Res. 2017;45:4655–66. https://doi.org/10.1093/nar/gkx114.
57. Jeandard D et al. Import of Non-Coding RNAs into Human Mitochondria: A Critical Review and Emerging Approaches. *Cells-Basel* 8, doi:ARTN 286. https://doi.org/10.3390/cells8030286 (2019).
58. Rubio MAT, et al. Mammalian mitochondria have the innate ability to import tRNAs by a mechanism distinct from protein import. P Natl Acad Sci USA. 2008;105:9186–91. https://doi.org/10.1073/pnas.0804283105.
59. Rubio MA, Hopper AK. Transfer RNA travels from the cytoplasm to organelles. Wiley Interdiscip Rev RNA. 2011;2:802–17. https://doi.org/10.1002/wrna.93.
60. Mercer TR, et al. The human mitochondrial transcriptome. Cell. 2011;146:645–58. https://doi.org/10.1016/j.cell.2011.06.051.
61. Magalhaes PJ, Andreu AL, Schon EA. Evidence for the presence of 5S rRNA in mammalian mitochondria. Mol Biol Cell. 1998;9:2375–82. https://doi.org/10.1091/mbc.9.9.2375.
62. Puranam RS, Attardi G. The RNase P associated with HeLa cell mitochondria contains an essential RNA component identical in sequence to that of the nuclear RNase P. Mol Cell Biol. 2001;21:548–61. https://doi.org/10.1128/Mcb.21.2.548-561.2001.
63. Prachar J. Intimate contacts of mitochondria with nuclear envelope as a potential energy gateway for nucleo-cytoplasmic mRNA transport. Gen Physiol Biophys. 2003;22:525–34.
64. Kamo N, Muratsugu M, Hongoh R, Kobatake Y. Membrane potential of mitochondria measured with an electrode sensitive to tetraphenyl phosphonium and relationship between proton electrochemical potential and phosphorylation potential in steady state. J Membr Biol. 1979;49:105–21. https://doi.org/10.1007/BF01868720.
65. Yoshinaga MY, Kellermann MY, Valentine DL, Valentine RC. Phospholipids and glycolipids mediate proton containment and circulation along the surface of energy-transducing membranes. Prog Lipid Res. 2016;64:1–15. https://doi.org/10.1016/j.plipres.2016.07.001.
66. Haines TH, Dencher NA. Cardiolipin: a proton trap for oxidative phosphorylation. FEBS Lett. 2002;528:35–9. https://doi.org/10.1016/s0014-5793(02)03292-1.
67. Chin K, Sharp KA, Honig B, Pyle AM. Calculating the electrostatic properties of RNA provides new insights into molecular interactions and function. Nat Struct Biol. 1999;6:1055–61. https://doi.org/10.1038/14940.
68. Mannella CA. Structure and dynamics of the mitochondrial inner membrane cristae. Biochim Biophys Acta. 2006;1763:542–8. https://doi.org/10.1016/j.bbamcr.2006.04.006.
69. Paumard P, et al. The ATP synthase is involved in generating mitochondrial cristae morphology. EMBO J. 2002;21:221–30. https://doi.org/10.1093/emboj/21.3.221.
70. Ikon N, Ryan RO. Cardiolipin and mitochondrial cristae organization. Biochim Biophys Acta Biomembr. 2017;1859:1156–63. https://doi.org/10.1016/j.bbamem.2017.03.013.
71. Cameron TA, Matz LM, De Lay NR. Polynucleotide phosphorylase: not merely an RNase but a pivotal post-transcriptional regulator. PLoS Genet. 2018;14:e1007654. https://doi.org/10.1371/journal.pgen.1007654.
72. von Ameln S, et al. A mutation in PNPT1, encoding mitochondrial-RNA-import protein PNPase, causes hereditary hearing loss. Am J Hum Genet. 2012;91:919–27. https://doi.org/10.1016/j.ajhg.2012.09.002.
73. Shimada E, et al. PNPase knockout results in mtDNA loss and an altered metabolic gene expression program. PLoS ONE. 2018;13:e0200925. https://doi.org/10.1371/journal.pone.0200925.

Publisher's note